A Trajectory Mapping Technique for the Visualization and Analysis of Three-Dimensional Flow in Supercell Storms

DANIEL P. BETTEN AND MICHAEL I. BIGGERSTAFF

School of Meteorology, University of Oklahoma, Norman, Oklahoma

LOUIS J. WICKER

NOAA/National Severe Storms Laboratory, Norman, Oklahoma

(Manuscript received 5 February 2016, in final form 7 October 2016)

ABSTRACT

A visualization technique that allows simultaneous spatial analysis of complex flow behavior from thousands of Lagrangian trajectories is presented and tested using a high temporal and spatial resolution cloud model. The utility of the trajectory mapping technique is illustrated by showing that the source height of the air trajectories is a good proxy to the model-derived equivalent potential temperature. Moreover, the history of the forcing of vertical momentum is related to instantaneous vertical motion patterns shown to be elucidated in the trajectory mapping framework. The robustness of the trajectory mapping method was evaluated by integrating tendency terms and comparing Lagrangian-derived quantities to instantaneous values in the model. The original trajectory maps were also compared to those where the original fields have been filtered and/or the available data frequency are limited to the spatial and temporal scales typical of research radar datasets. The trajectory mapping method was applied to a supercell observed on 29 May 2004 to demonstrate that trajectory behavior for the observed case compares well to those from the higher-resolution numerical model output.

1. Introduction

One of the most commonly used methods to characterize three-dimensional motion in complex flows is to examine Lagrangian trajectories. In supercell storms, conclusions about the behavior and source of low-level vortices in numerical simulations (Rotunno and Klemp 1985; Wicker and Wilhelmson 1995; Adlerman et al. 1999; Mashiko et al. 2009; Schenkman et al. 2014) and observational studies (Johnson et al. 1987; Wakimoto et al. 1998; Ziegler et al. 2001; Markowski et al. 2012) have been based, in large part, on the behavior of air trajectories. However, a recent study by Dahl et al. (2012) examined potential errors in individual backward trajectories that had been previously overlooked, indicating that trajectories originating at low levels east of a storm's gust front may have larger errors than other trajectories originating farther aloft. Thus, conclusions based on a limited set of trajectories may be biased due to undiagnosed local variability in trajectory errors.

Trajectories have been primarily visualized by overlaying the trace of parcel positions relative to the model or analysis grid at a specific analysis time. Variables along the trajectory, such as altitude, vertical vorticity, or forcing terms, from the vorticity equation are viewed as a time series. While helpful in illustrating key concepts in fluid motion, the evolution of specific features, the representativeness, and the spatial scales of the trajectory behavior cannot be determined from a few trajectories. With the exception of Klemp et al. (1981), who used trajectories to visualize the source altitude of air in a midlevel updraft, comprehensive analysis of trajectory behavior has not been thoroughly explored or visualized. For example, regions of strong deformation will lead to strong gradients in trajectory behavior that are difficult to visualize using only a few tens of trajectories. However, if thousands of trajectories are initialized on a fine, regularly spaced grid and analyzed in a Cartesian frame of reference, the resulting spatial pattern of trajectory behavior and diagnostics should lead to an improved understanding of storm kinematics and dynamics.

Corresponding author e-mail: Daniel Betten, danbetten@ou.edu

DOI: 10.1175/JTECH-D-16-0043.1

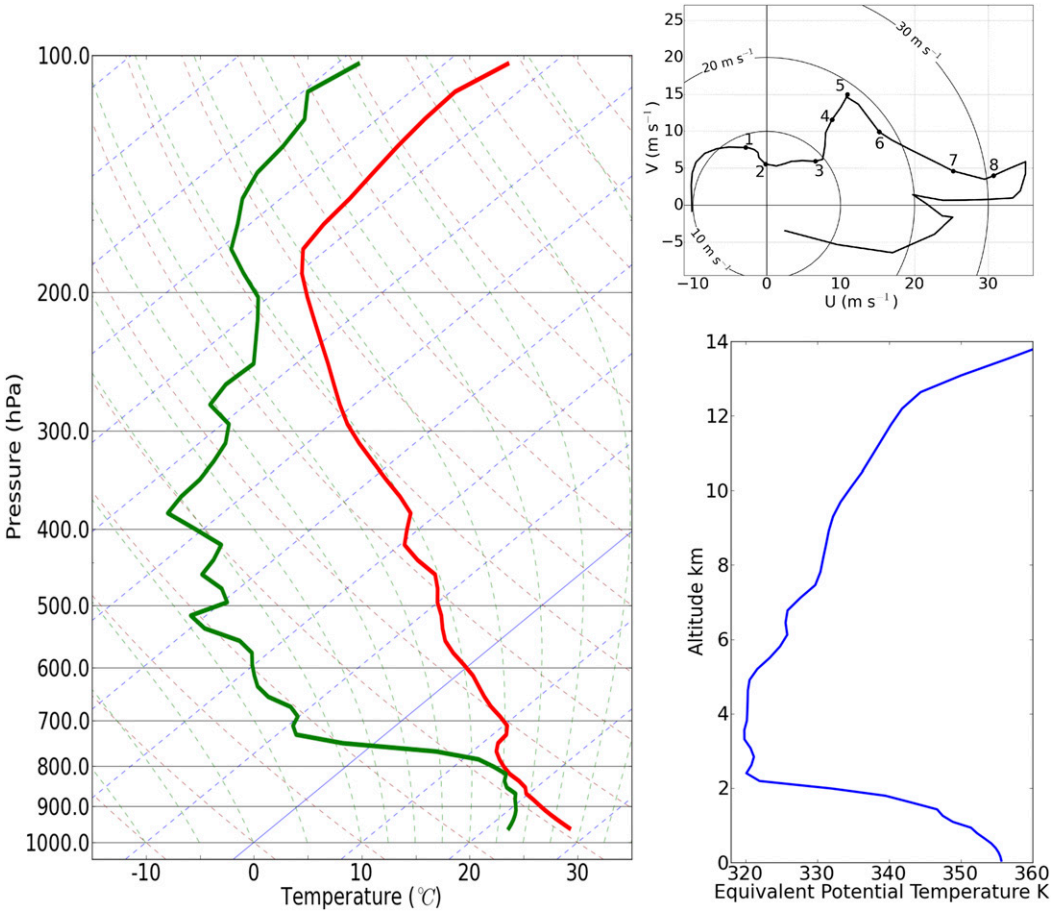

FIG. 1. (left) Thermodynamic profile, (top right) storm-relative hodograph (heights in km), and (bottom right) equivalent potential temperature profile (AGL) for the sounding used in the model. The sounding is a composite from the 1800 and 0000 UTC 8 May 2003 soundings at Topeka.

In this paper, we develop such a trajectory mapping method and demonstrate its robustness and utility using high-resolution output from a numerical model. The method will be shown to provide insight into the source of air parcels at a given level; the time history of vorticity, including the effects of diffusion; and the time-averaged forcing of vertical momentum. We also compare the trajectory behavior obtained from the simulated supercell storm to trajectories computed from a dual-Doppler radar analysis of a well-observed supercell storm. The comparison shows that the method has utility for an organized storm that is sampled frequently relative to the evolution of the storm flow.

2. Methodology

a. Numerical simulation

A numerical simulation was carried out using the Cloud Model 1 (CM1), release 17 (Bryan and Fritsch 2002), with the Ziegler variable density (ZVD; Ziegler 1985; Mansell et al. 2010) two-moment microphysics scheme. The simulation was initialized with a single warm bubble in a homogenous environment based on a composite sounding from Topeka, Kansas, for 8 May 2003 (Fig. 1). This sounding was chosen based on its proximity to multiple tornadic supercells. The sounding resulted in the simulation of a quasi-steady supercell storm, defined here following Foote and Frank (1983), as a continuous zone of updraft feeding the convective storm with new updraft pulses forming within the existing updraft zone. The weighted essentially nonoscillatory (WENO) advection scheme (Shen and Zha 2010) was applied for both kinematic and scalar quantities because it dampened errors associated with features near the smallest resolvable scale and resulted in smoother fields than the traditional fifth- and sixth-order advection schemes. The WENO method led to better agreement between integrated tendencies and the resulting field than fifth- or sixth-order advection schemes.

The horizontal grid spacing was 250 m in the middle 70 km of the domain and was stretched to 5000 m on the outer boundaries. The vertical grid spacing was stretched from 100 m at the bottom to 500 m at the top, resulting in a model domain of 175 km × 175 km × 16.2 km. The horizontal boundaries are open radiative, while the lower and upper boundaries are free slip. Storm motion was estimated and subtracted out to keep the storm in the middle of the domain over the lifetime of the simulation.

b. Observational case

The trajectory mapping technique was also applied to radar analyses from the Geary, Oklahoma, 2004 supercell observed by two Shared Mobile Atmospheric Research and Teaching (SMART; Biggerstaff et al. 2005) radars during the TELEX (MacGorman et al. 2008) project. Wind retrievals were performed using NCAR software REORDER (Oye and Case 1995) and Custom Editing and Display of Reduced Information in Cartesian Space (CEDRIC; Miller and Fredrick 1998) from synchronized radar volumes collected every 3 min. The radars were located on a 40-km baseline and an analysis was performed on a 100 km × 90 km × 18 km grid with a horizontal resolution of 750 m and a vertical resolution of 500 m. A low-pass filter was used to smooth the transition between the dual-Doppler analysis and a nearby balloon sounding. The storm advection correction technique described in Ziegler (2013), where the analysis at two times is advected to the time of the trajectory, was used to reduce errors in trajectories due to the large-scale advection of the storm.

c. Trajectory methodology

The trajectory algorithm used in this study was written to optimize the initialization of a regularly spaced grid of trajectories with fourth-order Runge–Kutta temporal integration. Trajectory time steps were based on the scale of the analysis and the resolved flow characteristics, resulting in a time step of 0.5 s for the simulated storm and 5 s for the observed storm. These time steps were found to be optimal, as smaller time steps did not affect the final positions or integrated quantities. Model data on the Arakawa C grid were directly interpolated to the trajectories using cubic spline interpolation, while the temporal evolution was linearly interpolated. The gradients were calculated locally by interpolating the variables to a cube around each trajectory and then calculating the spatial gradients valid at the center of the cube, thus ensuring that the gradients at the trajectory points are the same gradients that are felt by the trajectories.

Comparisons between forward and backward trajectories over 200 s using the algorithm developed here yielded root-mean-square differences on the order of 10 m, or about 5% of the grid spacing. The resulting algorithm also compared favorably against trajectories calculated from the built-in algorithm in CM1. Given the good agreement between forward and backward trajectories, the utility of the trajectory mapping framework is illustrated using mostly backward trajectories.

3. Trajectory map framework

A trajectory map is defined as a two-dimensional Cartesian visualization of a specific variable at a specific time along its trajectory. The trajectory maps are derived by initiating trajectories at every grid point on the original model or analysis grid and interpolating diagnostic quantities to the trajectory location during the backward (or forward) time integration. The trajectory map is then created by displaying the previous (or future) values of a quantity at the initial grid locations of individual trajectories. Hence, these maps reveal spatial patterns of the past (or future) values in the original two-dimensional plane.

To illustrate the transformation from Eulerian space to a trajectory map, the vertical velocity of trajectories at 1-km altitude is shown in Fig. 2. At the initial time (Fig. 2a), the trajectory map reflects the vertical velocity as indicated by the overlapping of the color-filled and black-lined contours of vertical motion. Figures 2b,c illustrate the horizontal variability of the past values of vertical motion for all the air parcels that end at 1-km altitude at 7200 s in the simulation. Thus, the spatial scale of the updraft intensification and the relative strengthening of the downdrafts can be visualized simultaneously. In contrast, single trajectories, like those in Fig. 2d, do not provide the spatial scale and structure of the air parcel evolution that is depicted in the trajectory maps.

The choice of the time, or integration period, depends on the purpose of the analysis, storm size, flow speed, and rate of evolution of the flow features of interest. For reference, the simulation produced a low-level updraft region ~5 km wide, while the observed supercell had an updraft region ~15–20 km wide. Thus, the observational case should require a significantly longer integration period than the simulated supercell for similar illustrative purposes. If the purpose is to gain a temporally comprehensive visualization of the vertical motion of air parcels, then one might plot the average vertical motion over a 50–100-s period rather than the instantaneous value at a specific time. On the other hand, if the purpose is to visualize parcel altitude origins, then one might plot the past altitude of the air that ended up at a particular altitude at a particular time in the simulation.

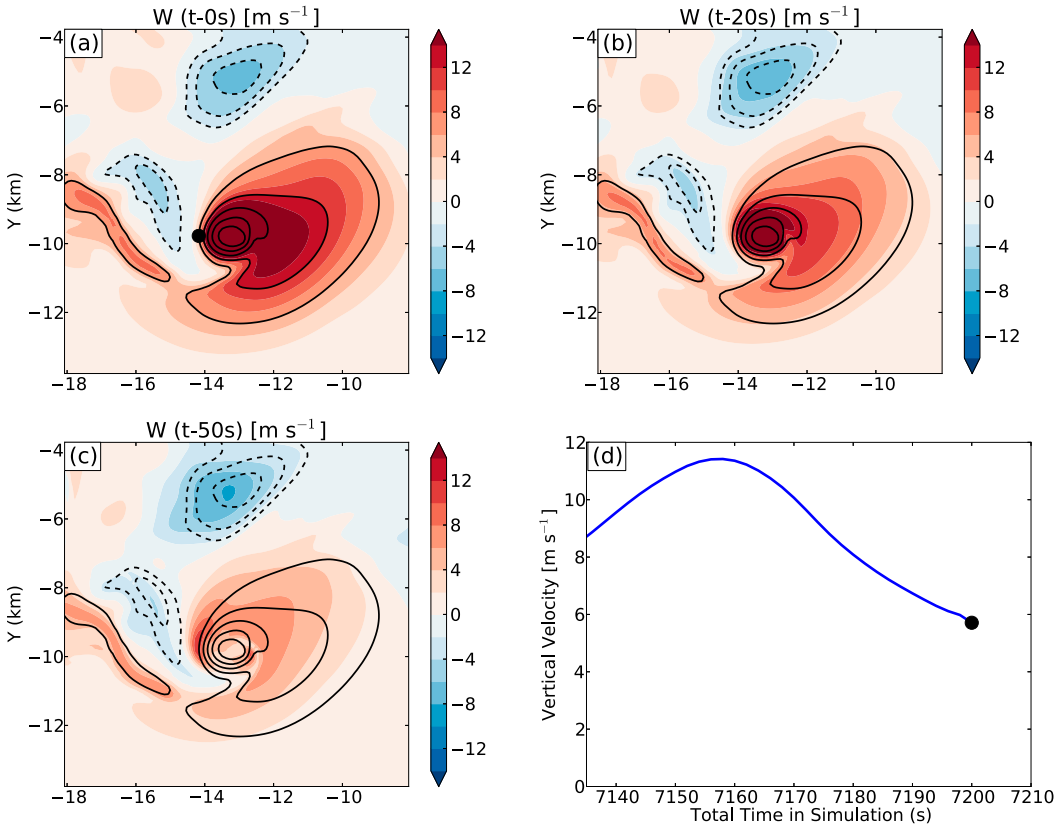

FIG. 2. (a) Vertical motion of 1 km at 7200 s into the simulation. (b) Horizontal map of vertical motion at 7180 s for all the backward trajectories that initiated at 1 km at 7200 s. (c) As in (b), but integrated back to 7150 s. In (a)–(c) black-lined contours of vertical motion every 2 m s^{-1} for negative values and 6 m s^{-1} for positive values at 1-km altitude and at 7200 s have been overlaid for reference. (d) Example of the time series of vertical motion along a single backward trajectory initiated at 7200 s at the point denoted by the black dot in (a).

For example, backward trajectories showing the prior altitude of air that end at 1-km altitude at 7200 s into the simulation are show in Fig. 3. As the trajectories are integrated backward in time, spatial gradients appear in regions having strong deformation as differential advection alters the path of individual trajectories (Fig. 3). In the trajectory mapping framework, the effects of deformation and flow evolution have been integrated into a single visual analysis. Instead of viewing fields such as vertical motion as a single snapshot in time on the horizontal grid, the trajectory mapping method enables the integrated time history of the flow field to be viewed concisely.

Some quantities will converge to a constant value along trajectories once they are reintegrated into the environment, such as source altitude. However, since the point in time of convergence depends on the initial trajectory position and the surrounding flow, the time of convergence will vary spatially. This point is illustrated in Fig. 3, where prior altitude has been plotted at four different times. Prior altitude converged first in regions of rising trajectories (warm colors) and took longer in regions with sinking trajectories (cold colors). Eventually, almost all of the backward trajectories that were initialized at 7200 s and at 1-km altitude converged to their source altitudes in the environment as the integration period was increased to 800 s.

It is important to note that both backward and forward trajectory maps contain useful insight into parcel flow evolution. Backward trajectory maps are optimal for understanding the processes that have forced the current flow characteristics, while forward trajectory maps are optimal for understanding the future behavior of the flow characteristics and for illustrating source regions for future updrafts, downdrafts, and flow features like mesocyclones.

4. Trajectory map applications

The benefit of the trajectory mapping framework is demonstrated here through analysis of quantities typically examined in studies of supercell storms. The source

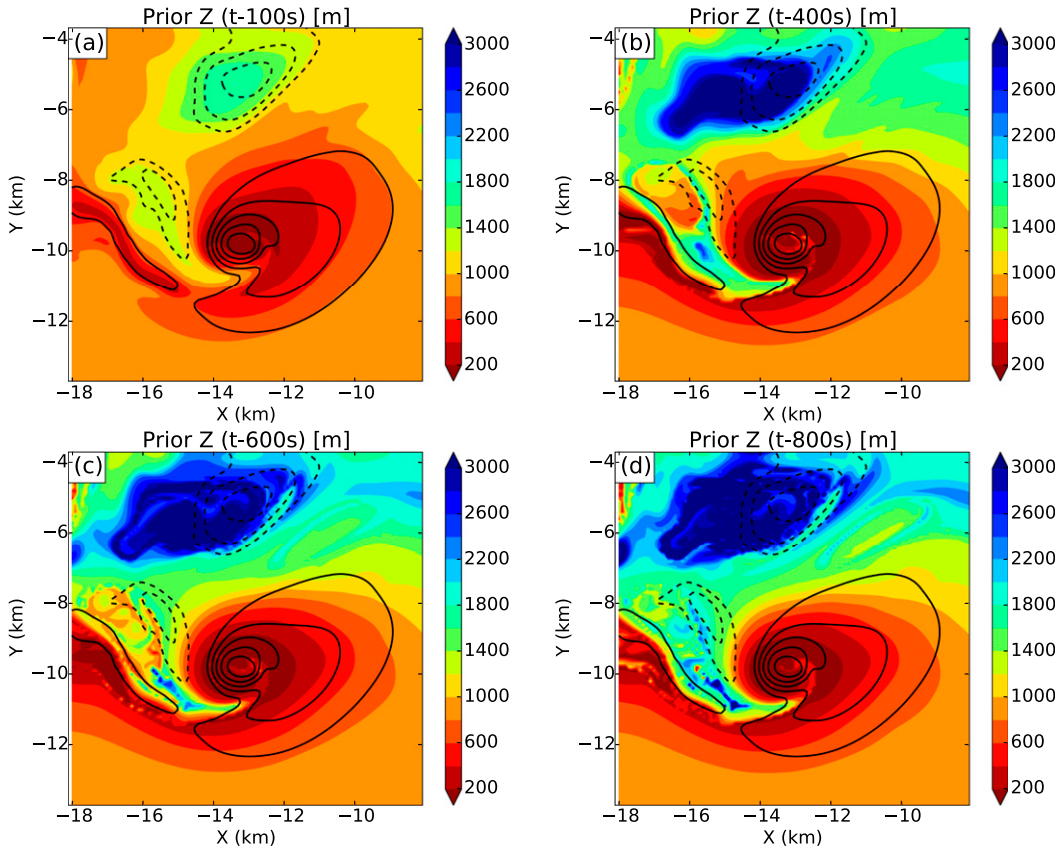

FIG. 3. (a) Prior altitude, 100 s in the past, initialized at 1-km altitude at 7200 s in the model simulation. (b) As in (a), but the backward trajectories have been integrated for 400 s. Note that points with a height of 1000 m indicate the parcel either did not move vertically or ended at 1-km altitude again between the beginning and ending periods of the integration. In (a) and (b), black contours of vertical motion every 2 m s^{-1} for negative values and 6 m s^{-1} for positive values at 1-km altitude and at 7200 s have been overlaid for reference.

of air in the low-level mesocyclone, the forcing of vertical momentum, and the developing vertical vorticity in and near the mesocyclone are presented for the simulated storm. The model output is also used to elucidate the proxies of observational applications where detailed thermodynamic data are often unavailable.

a. Low-level mesocyclone air source regions

To determine the horizontal extent of the areas that contributed to the low-level mesocyclone at a height of 1 km, a forward trajectory map was initiated at 7000 s at an altitude of 50 m. The selection of 50 m is illustrative but was guided by the mean vertical displacement within the mesocyclone found in the 200-s backward trajectory analysis (cf. Figs. 4a,b). In practice, many maps would be initialized at different altitudes within the height range diagnosed from the backward trajectory map. To reflect the broadest horizontal extent of air that was at 50-m altitude at 7000 s that could have flowed through the mesocyclone by 7200 s, the maximum vertical vorticity below 1 km along the forward trajectory is plotted (Fig. 4d) rather than the final vorticity. As with the prior altitude maps, the future maximum vertical vorticity was generated by contouring the future values of vorticity at the original (x, y) locations where the forward trajectories were initiated. While the future values in Fig. 4d are significantly larger than the initial vorticity values of the trajectories (Fig. 4c), this does not suggest that vorticity was increasing everywhere outside of the mesocyclone. Rather, the area of high future vorticity elucidates those individual forward trajectories that later pass through the low-level mesocyclone. The surface to the 1-km layer was chosen to focus on the low-level mesocyclone. Positive vertical vorticity values inside the low-level mesocyclone were significantly higher than any other region below 1 km in the simulation domain; thus, any air parcel trajectory that experiences future vertical vorticity on the same order of magnitude as that found in the mesocyclone—but originating outside of the mesocyclone—can be assumed to have passed through the low-level mesocyclone at some

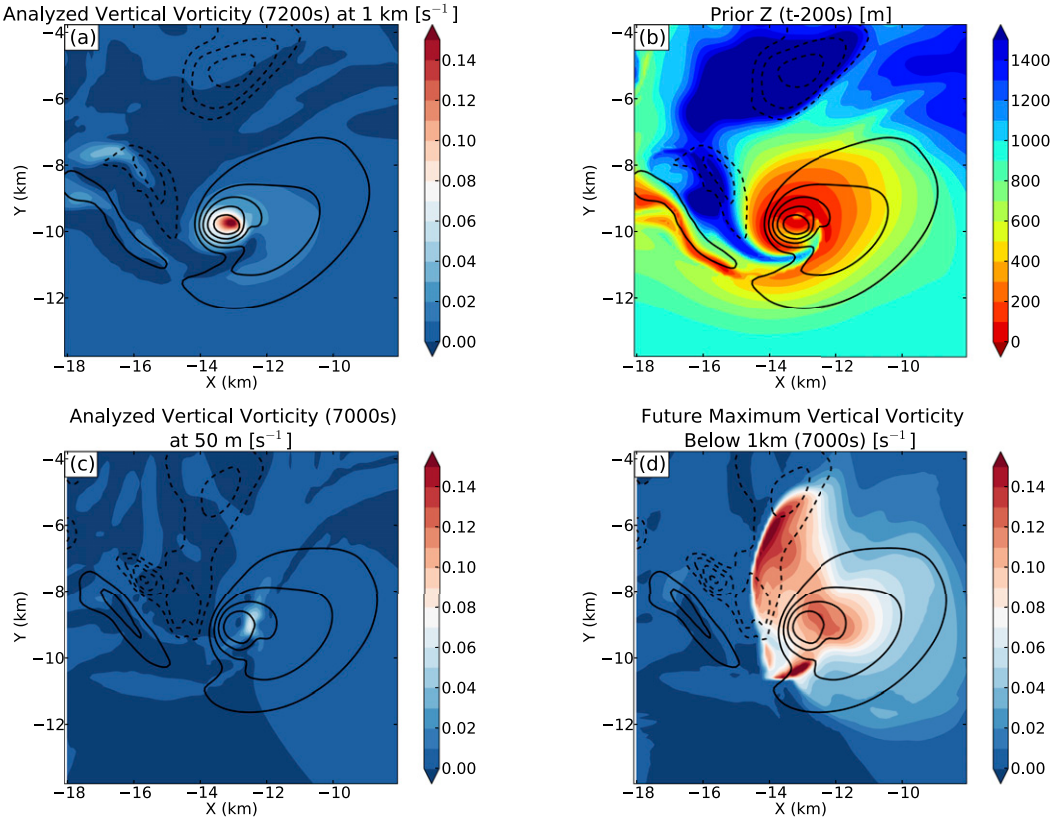

FIG. 4. (a) Analyzed vertical vorticity (s^{-1} according to the color scale) at 1-km altitude and 7200 s into the model simulation. (b) Prior altitude (m), 200 s into the past. Contours of vertical velocity, every 2 m s^{-1} for negative values and 6 m s^{-1} for positive values, for 1-km altitude at 7200 s have been overlaid in (a) and (b). (c) Analyzed vertical vorticity (s^{-1}) at 50-m altitude and 7000 s into the simulation. (d) Maximum vertical vorticity below 1-km altitude along 200-s forward trajectories initiated at 50 m at 7000 s into the simulation. The location of the color-filled contours reflects the grid points where the forward trajectories were initiated and not the future position at which the maximum vorticity values were realized. Contours of vertical velocity, every 2 m s^{-1} for negative values and 6 m s^{-1} for positive values, for 1-km altitude at 7000 s have been overlaid in (c) and (d).

point in the future. Examining the areas with values of vorticity greater than 0.06 s^{-1} (very light blue, white, and red in Figs. 4a,d), it is clear that air from several kilometers away in nearly all directions converged into the low-level mesocyclone between 7000 and 7200 s in the simulation. But the largest source area was from the north, in a region of general subsidence at both 7000 s (Fig. 4d) and 7200 s (Fig. 4a).

By comparing both backward and forward trajectories, it is possible to visualize the spatial distribution of the source height (for backward trajectories) and the horizontal source extent (from forward trajectories initialized at the earlier time) of air that contributed to the low-level mesocyclone at a particular time.

b. *Application to the forcing of vertical motion*

Trajectory maps have a large number of applications, as any variable that is observed or numerically simulated can be interpolated to a trajectory. Tendency equations are often used to elucidate the evolution of storm characteristics, such as vorticity or vertical motion. Individual or combined terms in tendency equations can be integrated and plotted just as easily as prior variable states. Hence, trajectory mapping can be used to examine the relation between past forcing and current flow features. As noted by Gaudet and Cotton (2006), advection will displace the resulting field from the parent forcing region. In their example, the occlusion downdraft was displaced from the location of the negative vertical motion tendency, showing the inherent complexity between the resulting motion field and the processes that created the flow.

The displacement between the forcing and the resulting momentum at later times can be demonstrated by comparing the vertical motion field to the rhs of the vertical motion tendency [(1)] and the Lagrangian integration of

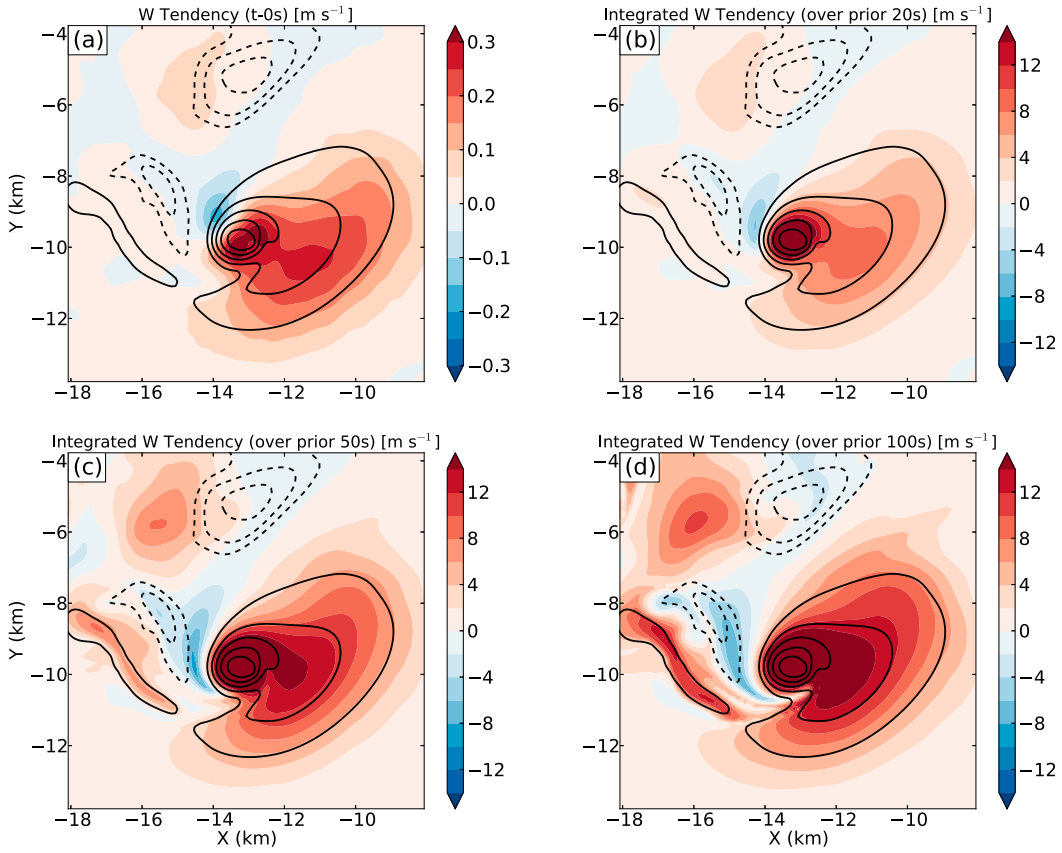

FIG. 5. (a) Instantaneous vertical velocity tendency (m s^{-2}) at 7200 s at 1-km altitude in the numerical simulation. (b) Vertical motion tendency from integration of the rhs of (1) along 20-s backward trajectories initialized at 7200 s at 1 km in the model. (c) As in (b), but for 50-s backward trajectories. (d) As in (b) and (c), but for 100-s backward trajectories. Black contours in every panel denote the instantaneous vertical motion every 2 m s^{-1} for negative values and 6 m s^{-1} for positive values at 7200 s at 1-km altitude in the model.

the terms over an arbitrary period (Fig. 5). Equation (1) is the compressible nonhydrostatic form of the vertical momentum equation in the numerical model, where w is the vertical velocity, t is time, π' is the perturbation Exner function, C_p is the heat capacity at constant pressure for air, g is acceleration due to gravity, z is height, θ_ρ is density potential temperature, and B is the buoyancy force defined by (2). As shown in (2) $\theta_{\rho 0}$ is the environmental base-state density potential temperature that varies only in height,

$$\frac{dw}{dt} = -\theta_\rho C_p \frac{\partial \pi'}{\partial z} + B \tag{1}$$

$$B = g\frac{(\theta_\rho - \theta_{\rho 0})}{\theta_{\rho 0}}. \tag{2}$$

Using the Emmanuel (1994) approximation for density potential temperature [(3)], the buoyancy force can be written as (4), where r_h is the hydrometeor mixing ratio, θ is potential temperature, and the virtual potential temperature θ_v was decomposed into its environmental base state θ_{v0} and perturbation θ_v'. Note that the environmental base-state virtual and density temperatures are equivalent, since there are no hydrometeors in the environment,

$$\theta_\rho = \theta_v - \theta r_h \tag{3}$$

$$B = g\left[\frac{\theta_v'}{\theta_{\rho 0}} - \frac{\theta}{\theta_{\rho 0}} r_h\right]. \tag{4}$$

At the initial time (Fig. 5a), the strongest drafts, particularly the downdrafts, are notably displaced from the peak tendencies. As the backward integration period is increased from 50 to 100 s, insight into the important timing of vertical motion tendency for the different vertical drafts at $t - 0$ becomes apparent. The updraft maximum in Fig. 5a is strongly forced for the entire previous 100 s. Additionally, the updraft band in Fig. 5a that extends from ($x = -18$ km, $y = -8$ km) to ($x = -16$ km, $y = -11$ km)

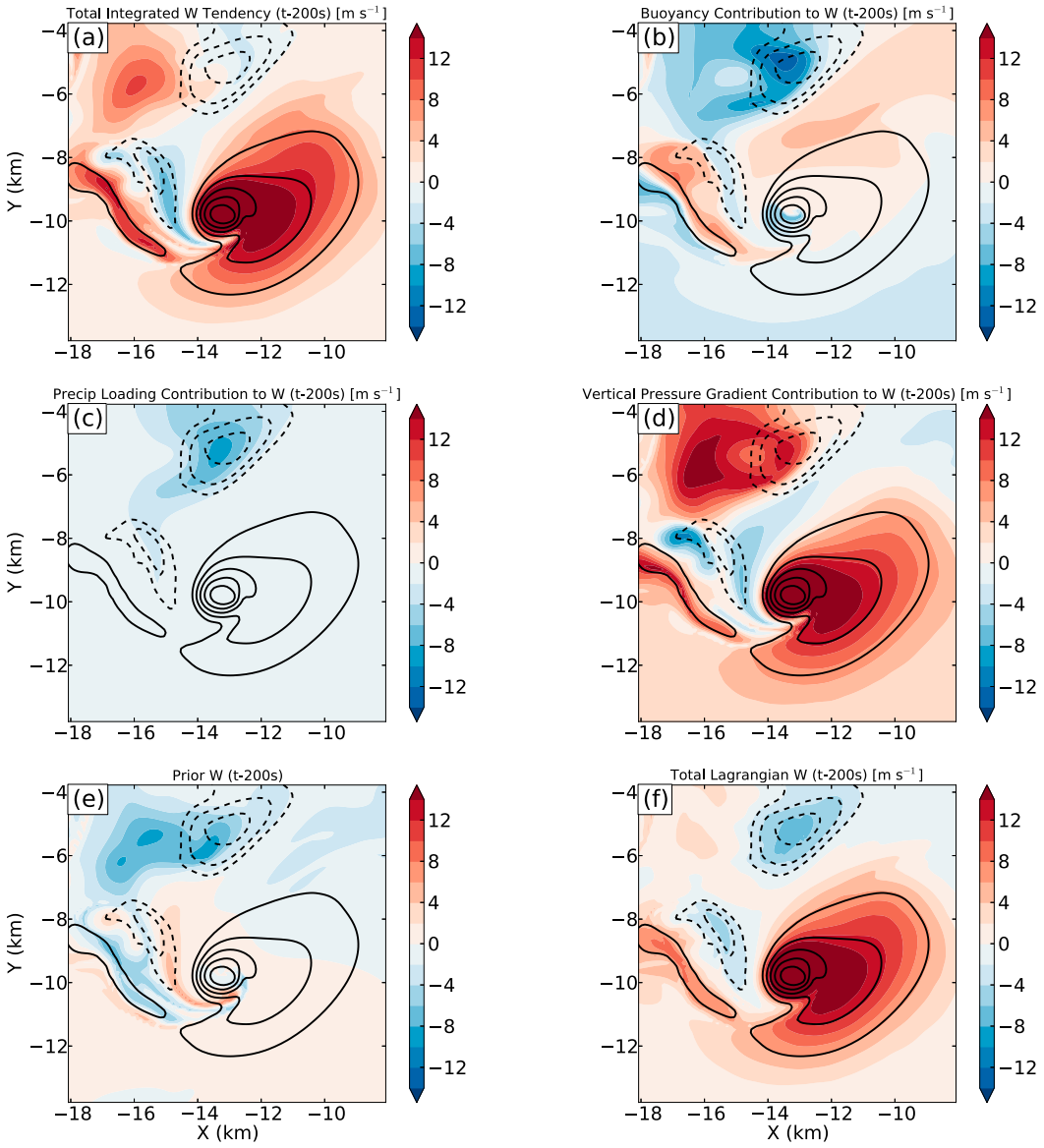

FIG. 6. Vertical motion tendency terms integrated backward 200 s from an initial time of 7200 s at 1 km in the model (color-filled contours). (a) The total tendency, (b) the contribution by buoyancy, (c) the precipitation loading term, and (d) the amount associated with the vertical pressure gradient force. (e) The vertical motion at 7000 s from backward trajectories initiated at 7200 s at 1 km. (f) The initial condition from (e) is used in the 200-s forward integration of the tendency equation along trajectories to produce the Lagrangian vertical motion, valid at 7200 s at 1-km altitude. Black contours in every panel denote the instantaneous vertical motion every 2 m s^{-1} for negative values and 6 m s^{-1} for positive values at 7200 s at 1-km altitude in the model.

was a residual draft accelerated between 50 and 100 s prior to $t - 0$. The same is true for the downdraft immediately east of the updraft band and for all the weak vertical drafts above $y > -7$ km. Hence, the trajectory maps can help illustrate the relative age of the vertical drafts by comparing the integrated forcing at different times from the backward trajectories, thereby revealing which drafts have been recently accelerated and which ones are merely coasting.

To establish the primary forcing mechanism for the updrafts and downdrafts, specific terms in the tendency equations were integrated along the trajectories. In Fig. 6, the terms of the vertical motion tendency equation have been integrated over a 200-s period and separated into the buoyancy (Fig. 6b) and vertical pressure gradient (VPG; Fig. 6d) contributions. The precipitation loading (Fig. 6c) contribution to buoyancy was also plotted. By comparing the contributors to vertical motion, regions

where forces support or oppose one another can be ascertained. Note that the Exner function formulation of the tendency equation implicitly contains the pressure contribution to buoyancy (Doswell and Markowski 2004) so that a small part of the buoyancy is contained in the vertical pressure gradient. Additionally, the VPG has not been separated into dynamic and buoyant contributions (Rotunno and Klemp 1982). Thus, while both buoyancy (Fig. 6b) and the VPG (Fig. 6d) resulted in forcing of vertical motion, they largely negated each other in some areas.

For example, consider the forcing terms for the rear-flank downdraft (Ludlam 1963; Lemon and Doswell 1979; Klemp and Rotunno 1983) centered at ($x = -13.5$, $y = -5.5$ km) in Fig. 6a. It is clear that precipitation loading (Fig. 6c) and negative buoyancy (Fig. 6b) counters the mostly positive vertical pressure gradient force (Fig. 6d) to increase the downdraft strength from its initial value at $t - 200$ s (Fig. 6e). The northwest–southeast-oriented downdraft band at ($x = -15$ km, $y = -9$ km) is separated from the main downdraft region and was primarily forced by a negative VPG, similar to occlusion downdrafts simulated by Klemp and Rotunno (1983), Wicker and Wilhelmson (1995), and Adlerman et al. (1999). In contrast, the northwest–southeast-oriented updraft band from (x, y) of (-18 km, -8 km) to (-15 km, -11 km) in Fig. 6a was forced by a combination of buoyancy (Fig. 6b) and VPG (Fig. 6d). Meanwhile, the main updraft was forced almost entirely by the VPG.

For an observationally based dataset, vertical draft forcing could be difficult to diagnose due to the lack of pressure and thermodynamic information. Nonetheless, one could estimate the hydrometeor mixing ratio from radar reflectivity and thus integrate the precipitation loading contribution over trajectories (Wakimoto et al. 1998). This technique might differentiate downdrafts in the hook echo region that are dynamically driven from those that are more buoyancy driven by precipitation loading.

The robustness of the trajectories can be further tested by comparing the simulated vertical motion in the model (black contours) to the vertical motion obtained by starting at $t - 200$ s and integrating the tendency terms forward. Figure 6e shows the past vertical motion at $t - 200$ s for all the trajectories that end at 1-km altitude at 7200 s into the simulation. Starting with these vertical motions and integrating the vertical motion tendencies along the trajectories produces the color-filled plot of vertical motion in Fig. 6f. Even after 200 s, there is very strong agreement between the vertical motion obtained through forward integration of the tendencies and the instantaneous vertical motion, denoted by the black contours, at $t - 0$. Thus, the trajectory mapping analysis of vertical motion tendency is robust for this simulation over at least 200 s.c. Application to the forcing of vertical vorticity.

The vertical vorticity equation in height coordinates is given in (5), where ζ is relative vertical vorticity; t is time; f is the Coriolis parameter; u is the zonal component, v is meridional component, w is the vertical component of velocity; ρ is density; P is pressure; and, F_U and F_V are the diffusive tendencies in u and v, respectively,

$$\frac{d\zeta}{dt} = \underbrace{(f+\zeta)\left(\frac{\partial u}{\partial x}+\frac{\partial v}{\partial y}\right)}_{\text{Stretching}} + \underbrace{\left(\frac{\partial u}{\partial z}\frac{\partial w}{\partial y}-\frac{\partial v}{\partial z}\frac{\partial w}{\partial x}\right)}_{\text{Tilting}} + \underbrace{\left(\frac{\partial F_V}{\partial x}-\frac{\partial F_U}{\partial y}\right)}_{\text{Diffusion}} + \underbrace{\frac{1}{\rho^2}\left(\frac{\partial \rho}{\partial x}\frac{\partial P}{\partial y}-\frac{\partial \rho}{\partial y}\frac{\partial P}{\partial x}\right)}_{\text{Solenoidal}}. \quad (5)$$

The solenoidal term in (5) was several orders of magnitude less than the other terms and hereafter is neglected.

The diffusion term in (5) combines the effects of subgrid-scale turbulent mixing (Smagorinsky 1963) and numerical diffusion associated with the model advection scheme. Fortunately, CM1 has the option to output the exact turbulent mixing diffusion and a simplified approximation of the numerical diffusion. The numerical diffusion estimate is based on a single forward time step assuming a fifth-order advection scheme. In reality, the model goes through three small time steps over the same period and uses a WENO advection scheme, integrating the three time steps using a third-order Runge–Kutta method (Shen and Zha 2010). The exact determination of numerical diffusion from the WENO scheme is beyond the scope of this study. The simplified approximation obtained from CM1 is likely an underestimate of the true amount of numerical diffusion implicit in the simulation. Total diffusion was calculated separately from the other terms on the rhs of (5) to isolate its effect on the change in vorticity and because diffusion estimates are not readily available in most observational studies.

Unlike the tendency equation for vertical motion, the vertical vorticity equation is not a separable differential equation. Instead, (5) must be integrated, starting with an initial value for ζ and then using the prior value of ζ in the current estimate of the stretching term. A fourth-order Runge–Kutta integration method was used in calculating (5) along trajectories to mitigate error during periods of exponential ζ growth. In the discussion section to follow, *integrated vertical vorticity* refers to the integration of only the tilting and stretching terms in (5) over an arbitrary period. *Lagrangian vertical vorticity* refers to the integrated vertical vorticity plus the initial value of vertical vorticity at that point in the past.

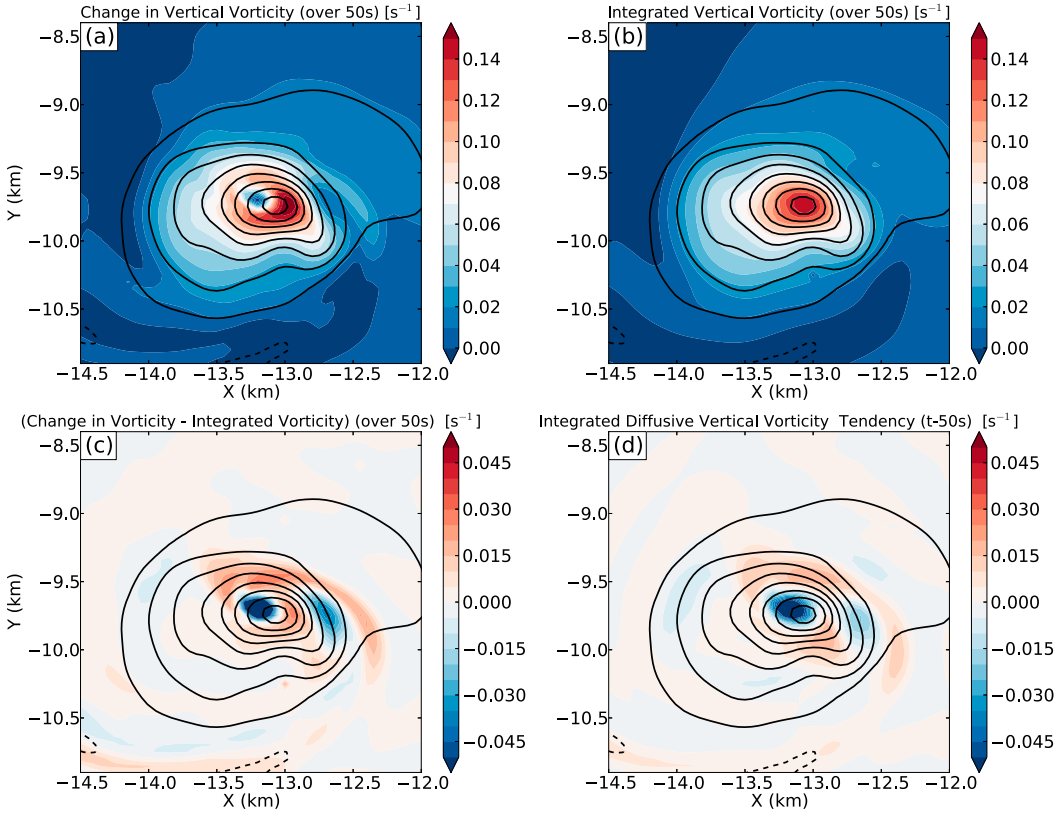

FIG. 7. Application of backward trajectory mapping to vertical vorticity analysis. (a) Total change in vertical vorticity [lhs of (2), s^{-1}] according to the color scale, for a 50-s backward trajectory initialized at 7200 s at 1-km altitude in the simulation. (b) Integrated vertical vorticity, from tilting and stretching alone, along 50-s backward trajectories. (c) The difference found by subtracting (b) from (a). (d) Integrated change in vorticity from diffusion, including both subgrid-scale turbulent mixing and the simplified numerical diffusion estimate, along 50-s backward trajectories. For reference, in each panel vertical vorticity at 7200 s at 1-km altitude has been contoured in black every 0.02 s^{-1}.

Backward trajectory analyses over a 50-s period initiated at 7200 s and 1 km in the simulation (Fig. 7a) show that the total change in vertical vorticity [the lhs of (5)] was mostly positive, especially in the mesocyclone. There is generally in good agreement between the total change in vorticity along the backward trajectories and the integrated vertical vorticity over the same period (Fig. 7b), suggesting that tilting and stretching were the dominant terms in the vorticity equation. However, near the vortex center (−13.3 km, −9.6 km in Fig. 7a), the average difference (Fig. 7c) approached 50% of the total change. Indeed, large differences—both positive and negative—were found in most regions where the vorticity gradient itself was large. To determine whether these differences were due to the total diffusion (subgrid-scale turbulent mixing plus numerical diffusion), total diffusion was calculated along the same backward trajectories (Fig. 7d). A residual vorticity term R was also constructed according to (6). Term R represents the actual total diffusion in the model, since the solenoidal term is small in comparison,

$$R = \frac{d\zeta}{dt} - (f+\zeta)\left(\frac{\partial u}{\partial x} + \frac{\partial v}{\partial y}\right) - \left(\frac{\partial u}{\partial z}\frac{\partial w}{\partial y} - \frac{\partial v}{\partial z}\frac{\partial w}{\partial x}\right). \quad (6)$$

Considering the difference between the simplified estimate of numerical diffusion and the actual numerical diffusion in the model, the agreement between the change in vorticity residual [lhs in (6); Fig. 7c] and the estimated changes associated with total diffusion (Fig. 7d) are remarkable. The spatial patterns of positive and negative regions are nearly collocated. The main discrepancy is that the magnitude of the estimated diffusion appears to be low. Interestingly, sensitivity tests in which the WENO advection scheme was replaced with a fifth-order advection scheme or even a fully explicit sixth-order advection scheme resulted in greater differences between the total diffusion using the simplified numerical estimate from CM1 and the residual vorticity change in Fig. 7c. Therefore, while the estimated total diffusion using the explicit turbulent mixing diffusion and the simplified numerical diffusion from release 17 of the CM1 model underestimates the amount of diffusion actually

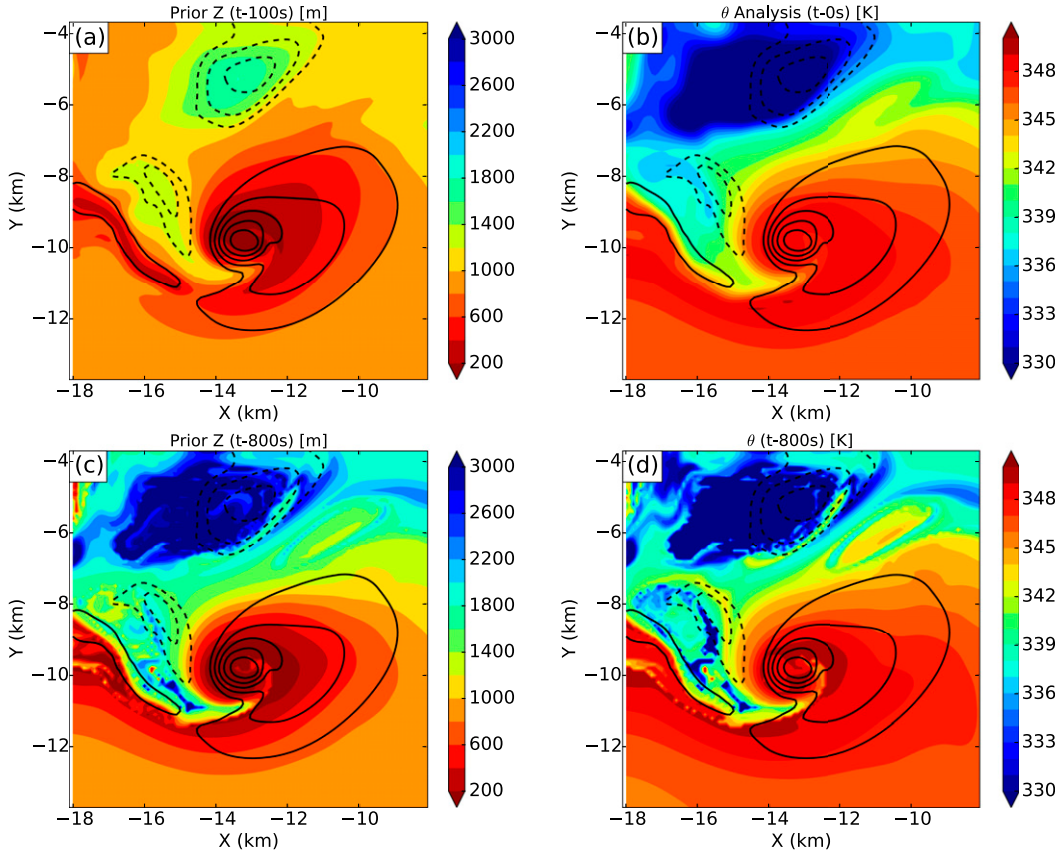

FIG. 8. Prior altitude after (a) 100 and (c) 400 s, (b) equivalent potential temperature at 0 s, and (d) prior equivalent potential temperature at 400 s, with analyzed vertical motion (black every 2 m s^{-1} for negative values and 6 m s^{-1} for positive). The trajectories were initiated at 7200 s at 1-km altitude in the model.

occurring in the model, the estimated total diffusion does explain the bulk of the discrepancy between the total change in vorticity along the backward trajectories and the integrated vertical vorticity.

The close agreement between the estimated total diffusion (Fig. 7d) and the residual vorticity change (Fig. 7c) suggests that the trajectory mapping technique itself did not introduce significant errors into the vorticity analysis. More importantly, the spatial pattern of diffusion can be elucidated by trajectory mapping. This may be the first time that the effects of diffusion on the vorticity field have been quantified within a simulation over the entire mesocyclone. Regions where the impact of diffusion is large would correspond to regions where unguided analysis of individual trajectories could lead to misinterpretations of the model vorticity budget along the trajectory.

d. Proxies for observational applications

Often in observational cases, only the kinematic properties of the storm are observed. Thus, thermodynamic properties and behavior have to be inferred from the kinematics. Trajectory mapping can be a useful tool to evaluate the utility of observable quantities that may be used as a proxy for basic thermodynamic structure. The quantity that will be examined here is source height, which will be shown to be a proxy for equivalent potential temperature θ_e as suggested by Markowski et al. (2002) because it is conserved for reversible moist adiabatic processes.

In most observational studies, θ_e is not available within the storm system. Thus, this proxy must be evaluated in the numerical simulation. In Fig. 8, prior altitude at 100 and 800 s is compared to θ_e at $t - 0$ and 800 s along trajectories. Over the shorter period, prior altitude is indicative of the recent vertical motion history of trajectories and suppresses the impact of past transient updrafts and downdrafts on the interpretation of the true source altitude of the trajectory. However, once the trajectories are traced back long enough—in this case 800 s—prior altitude (Fig. 8c) can then be considered a good qualitative proxy for θ_e. The required trajectory integration period is dependent on the scale of motion and magnitude of the flow. In this case, it is 800 s. But for

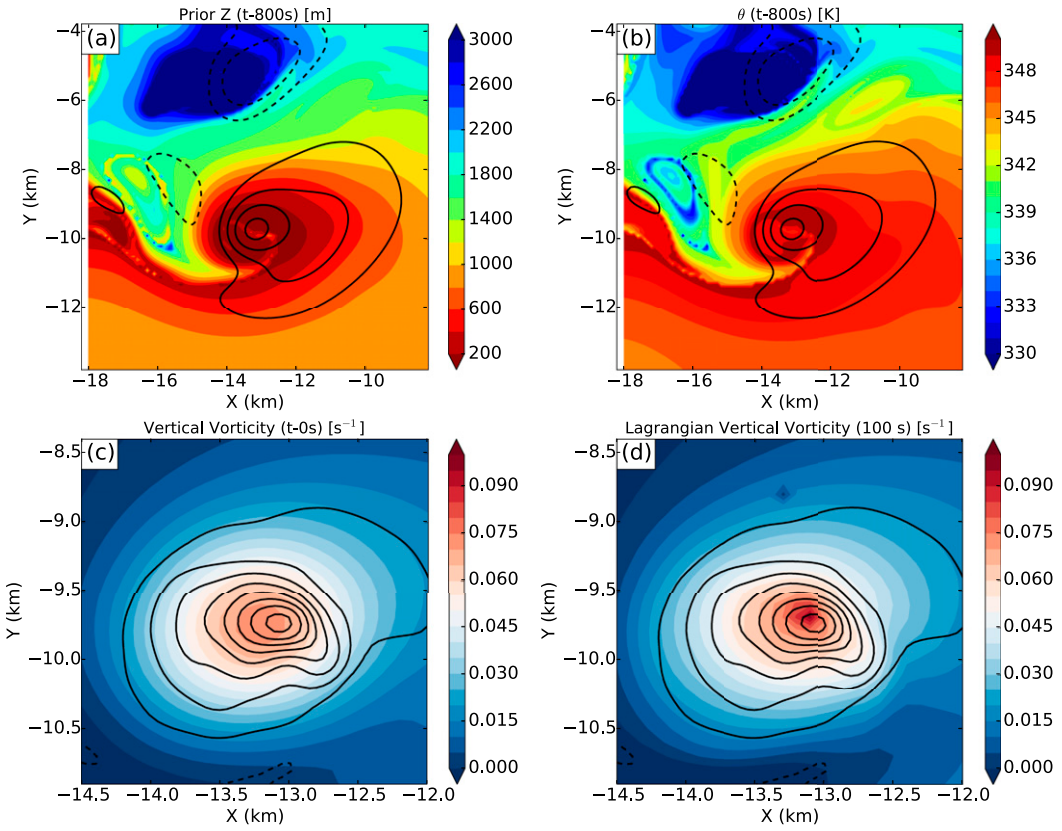

FIG. 9. Results after spatial filtering has been applied with a data frequency of 2 s. (a) Prior altitude and (b) equivalent potential temperature after 400 s of trajectory integration, with analyzed vertical motion (black every 2 m s^{-1} for negative values and 6 m s^{-1} for positive). (c) Analyzed vertical vorticity and (d) Lagrangian vertical vorticity after 100 s, with the original analyzed ($t - 0$) vertical vorticity (black contours every 0.02 s^{-1}) overlaid.

larger storms, the integration period could be more than 1500 s.

5. Sensitivity to observational sampling

Trajectory maps have been shown to be useful in elucidating the spatial pattern of fluid behavior in a numerical model when data are available at every time step and at every grid point. Observational datasets typically have coarser temporal and spatial resolution. For instance, mechanically scanning research radar volumetric scans of convective storms often require 2–3 min and have horizontal wavelength resolutions of 1–2 km (e.g., Lund et al. 2009; Bruning et al. 2010; Palucki et al. 2011). To determine the impact of sparse and infrequent data on trajectory maps, sensitivity tests were conducted using the model framework.

a. *Spatial-resolution test*

The effect of spatially undersampling storm structure was examined by applying a Gaussian filter ($\sigma = 1.5$) over horizontal planes in the numerical model output. The filter essentially removed energy at wavelengths less than 4 times the horizontal grid spacing, or less than 1 km for the 250-m-resolution model grid. Coarse spatial resolution did not appreciably influence 800-s backward trajectories of prior altitude or prior θ_e (cf. Figs. 9a,b with Figs. 8c,d). The filtered model output produced smoother trajectory maps with lower-amplitude extrema. But the physical behavior of the source region for the primary vertical draft was preserved, as was the scale of the downward-moving air that intruded into the west (left) side of the mesocyclone.

To test the significance of course resolution on the trajectory map of vertical vorticity changes, the Lagrangian vertical vorticity field over 100-s backward trajectories was computed. The final Lagrangian-derived vertical vorticity map is found by integrating (2) without the solenoidal and diffusion terms and by adding the initial vorticity at the beginning of the trajectory. Since the result depends on the filtered initial vorticity, only the effects from the Gaussian filter on the initial high-resolution vorticity are shown in Fig. 9c. Note that the filtered initial condition has lower amplitude, smoother structure, and a

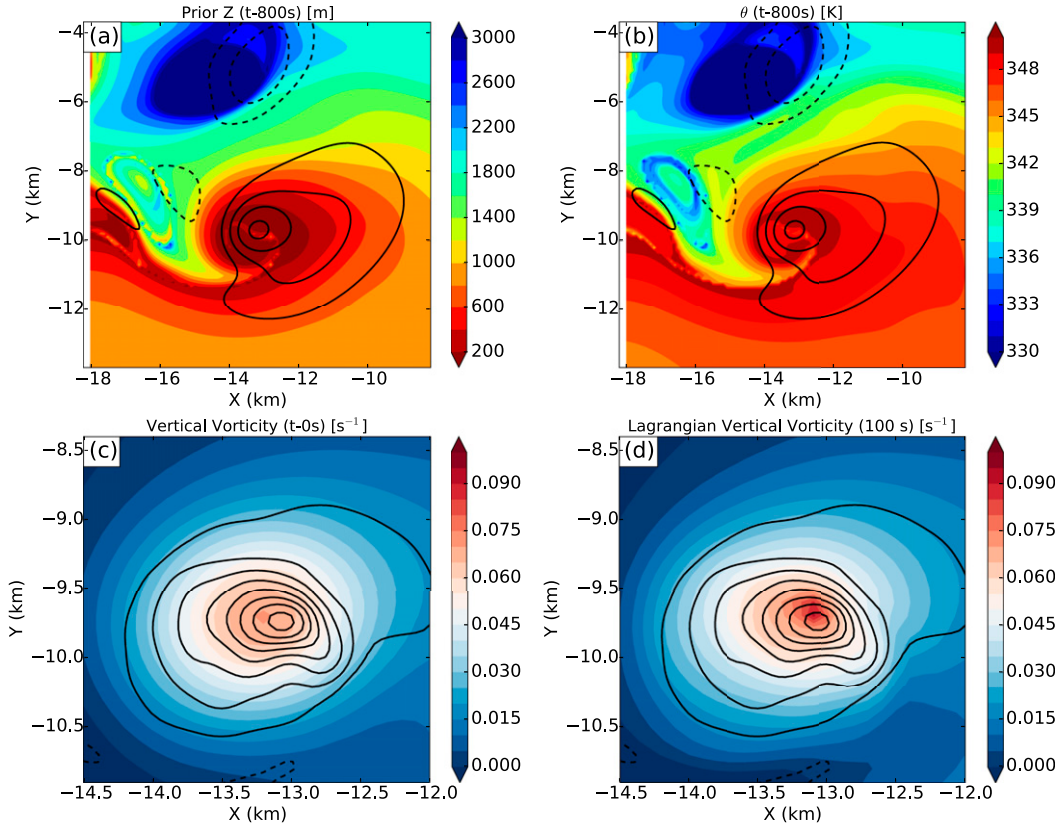

FIG. 10. As in Fig. 9, except that in addition to the spatial scale being smoothed, the model output frequency has been reduced to 180 s.

maximum that is displaced to the west (left) of the original high-resolution vortex. The Lagrangian vertical vorticity map, computed from 7100 to 7200 s into the simulation (Fig. 9d), resulted in sharper gradients, high-peak amplitude, and a smaller displacement of the vortex center than the filtered initial condition. Indeed, the Lagrangian vertical vorticity map is very similar to the original high-resolution vorticity at 7200 s. The mapped Lagrangian vertical vorticity responded to the same large-scale deformation that had caused the vortex in the model to become concentrated. Thus, mapping the Lagrangian-derived vertical vorticity recovered some of the structure in the vorticity field that was removed by the filter.

The impact of low spatial resolution but high temporal resolution is especially germane to observations collected with phased array radars (Heinselman et al. 2008; Isom et al. 2013; French et al. 2014). Phased array systems provide data every few seconds but with a spatial resolution comparable to, or slightly worse than, existing mechanically scanning weather radars. Hence, trajectory mapping analyses help improve the intrinsic resolvable spatial scale of fluid behavior and better match the frequency obtained from phased array radar observations.

b. *Combined spatiotemporal-resolution test*

To evaluate the trajectory mapping technique relative to more commonly available radar datasets from mechanically scanning radars, the filtered model output was further degraded by reducing the temporal resolution of the model output to 180 s. The trajectory location between time steps was computed using the advection correction scheme described in Ziegler (2013).

Limiting the temporal resolution of the filtered model output to 180 s resulted in little additional loss of fidelity in the 800-s backward trajectory maps of prior altitude and θ_e (cf. Figs. 10a,b with Figs. 9a,b). Indeed, the greatest impact on the trajectory map structure was due to coarse spatial resolution rather than limited temporal resolution of the data used in computing the trajectories. Regardless, even for the relatively poor temporal and spatial scales associated with currently available radar observations, the trajectory maps revealed the history and thermodynamic characteristics of the vertical drafts quite well.

The Lagrangian vertical vorticity map also did not suffer much additional change in trajectory behavior from the limited temporal sampling (cf. Fig. 10d with Fig. 9d). The resolved scale and spatial pattern of the trajectory map was very similar to that for just the degradation in spatial resolution. The deformation in the flow along the trajectories acted to sharpen the horizontal gradients, increase the magnitude of the extrema to better match the actual maxima, and helped force the vortex center to be closer to the actual vortex center at 7200 s as compared to the initial condition (Fig. 9c, 10c).

For the storm circulation examined here, which is of a size (2–3 km in diameter) and duration (~10 min) that are common to observed classic supercell storms (Burgess et al. 1982), the trajectory mapping analysis of the flow behavior was not significantly impacted by limiting the data to the resolution typical of wind retrievals for research radars.

Nevertheless, there were areas that showed sensitivity to sampling resolution. The prior altitude values exhibited small-scale variability in the rear-flank downdraft region to the west of the mesocyclone (cf. near $X = -16$, $Y = -9$ km in Fig. 8c). The variability in prior altitude was related to a small region of deformation associated with counterrotating vortices to the west of the mesocyclone and outside the area of precipitation at earlier times. Air that later arrived within this part of the rear-flank region was composed of a mixture of air that passed through or between these vortices. The lower spatial and temporal resolution trajectory maps of prior altitude (Figs. 9a, 10a) did not capture the subtlety of this flow and hence did not exhibit as much variability in this region. Instead, the lower-resolution sampling resulted in an averaged structure. In that manner, the lower-resolution sampling resulted in errors relative to the higher-resolution trajectory maps. But these errors do not appear to be dynamically significant to the storm's evolution.

Moreover, the trajectory mapping framework better defines the intrinsic spatial scales of the observed flows that help match gains in temporal resolution achieved by phased array radars. In general, the steadiness and scale of the dominant flow characteristics relative to the resolution of the observational sampling is a fundamental factor in the success of the trajectory mapping method in diagnosing internal storm behavior. For storms in which the flow is more transient or significantly undersampled spatially, the consistency of the deformation and thus the trajectory behavior can be expected to be more sensitive and the resulting analyses to have larger errors.

6. Observed supercell trajectory maps

The sensitivity tests in the previous section indicate that that backward trajectory maps should reveal the spatial pattern of air behavior in storms observed at 2–3-min intervals with spatial resolutions of 1–2-km wavelengths. A high-precipitation supercell was observed at those scales by the two SMART radars (Biggerstaff et al. 2005) during TELEX-2 (MacGorman et al. 2008) on 29 May 2004. Payne et al. (2010) and Calhoun et al. (2013) studied the polarmetric and lightning characteristics, respectively, of the storm with regard to its kinematics diagnosed from dual-Doppler wind retrievals. The wind retrievals have been extended to cover about a 75-min period at about 150-s intervals.

Prior altitudes over a period of 1000 s were determined using backward trajectories initiated at 1-km altitude at three different times to illustrate the spatial pattern of the airflow around the low-level mesocyclone (Fig. 11). The prior altitude maps appear similar to the simulation, with the biggest exception being the larger scale of the observed high-precipitation mesocyclone. At 1000 s before 0024 UTC 30 May 2004 (Fig. 11a), the air that eventually filled the mesocyclone at 1-km altitude came primarily from lower levels. However, there were small regions within the mesocyclone that contained air from above 1 km. This air had been transported in a small downdraft near the vortex center. Later, this air flowed around the vortex and mixed with air from altitudes closer to 1 km (Fig. 11b).

Outside the mesocyclone, evidence of a rainy downdraft (Brandes 1978) prior to 0024 UTC was observed to the northwest (upper-left area in Fig. 11a). Air from the rainy downdraft mixed with air from a stronger rear-flank downdraft that occurred before 0036 UTC, as indicated by the larger area of higher-altitude sources to the west and northwest of the vortex center at that time (Fig. 11b). These downdrafts did not cause the mesocyclone to occlude. However, their arrival appears coincident with the concentration and symmetrization of the mesocyclone, suggesting that the downdrafts helped to organize the low-level mesocyclone (cf. Figs. 11a,b). A much stronger downdraft occurred prior to 0048 UTC (Fig. 11c) in the southeastern sector of the mesocyclone. The sharp gradient in the pattern of prior altitude helps delineate the location of the rear-flank gust front at 0048 UTC. Compared to the earlier times, the gust front had clearly surged ahead of the mesocyclone at 1-km altitude, typical of the initial shape of a mesovortex occlusion process (Burgess et al. 1982; Dowell and Bluestein 2002) Similarly, the analyzed vertical vorticity at 0048 UTC became amplified as the low-level mesocyclone was stretched, consistent with trajectories originating from a level below 200 m.

The method of mapping Lagrangian trajectories in an Eulerian framework to better visualize the spatial scale and airflow behavior yields valuable insight into the

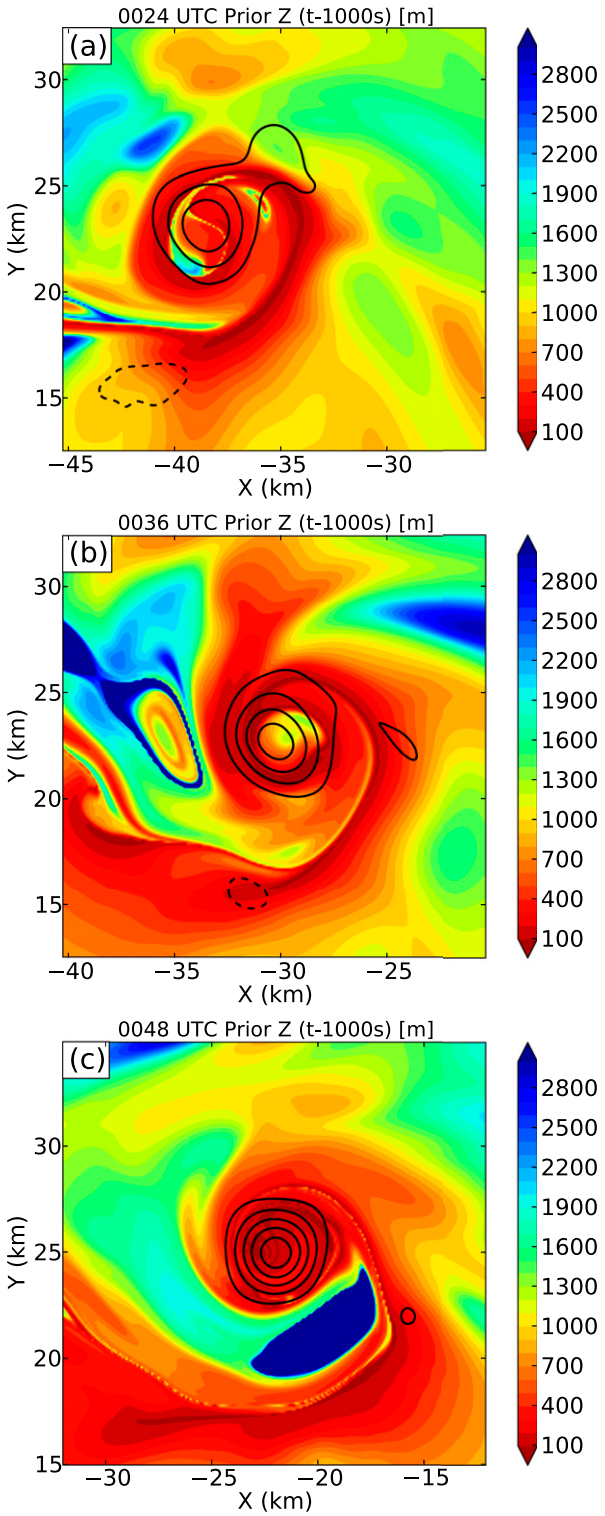

FIG. 11. Backward trajectory maps at 1000 s initiated at 1-km altitude from the 29–30 May 2004 Geary dual-Doppler wind retrievals. Prior altitude at 1000 s in the past (color-filled contours) is plotted for trajectories initiated at (a) 0024, (b) 0036, and (c) 0048 UTC 30 May. Analyzed positive vertical vorticity at each analysis time is contoured in black (every 0.01 s^{-1}).

mesocyclone evolution that is difficult to discern from individual dual-Doppler analyses. More importantly, given that deformation within this storm was quasi steady over the entire analysis period, the backward trajectory map clearly delineated the gradients separating different source regions of air that were observed at 1-km altitude near and within the mesocyclone. Hence, trajectory maps can be an invaluable tool that aids the understanding of observed storm evolution at a higher resolution than the individual analyses used to construct the maps. Future studies based on trajectory map analysis will focus on the role of downdrafts on the mesocyclone evolution and will extend the method to less steady multicell convective systems.

7. Discussion and conclusions

A trajectory mapping framework similar to Klemp et al. (1981) has been presented and demonstrated to improve the robustness of analyzed characteristics of fluid flows and to eliminate the need to generalize fluid motions through a small set of select trajectories. While the examination of individual Lagrangian trajectories has been a vital tool in understanding both observed and numerically simulated thunderstorms, they are subject to questions of representativeness and accuracy, especially those computed from observations. Backward trajectory maps have been shown to vividly illustrate the potential errors in randomly choosing a trajectory based on vertical velocity or vorticity due to deformation zones that cause gradients in trajectory behavior significantly smaller than the grid spacing. Although there is still value in examining individual trajectories, the trajectory mapping framework provides a more robust perspective and an invaluable sense of representativeness that would not be available otherwise.

One important caveat is the choice of integration periods presented in this paper. The spatial structure and scale of trajectory behavior is completely dependent on the scales of motion and deformation. An integration period of 100 s could be sufficient for a region of small-scale motion, while a similarly structured but much larger scale of motion could require an integration period of 500 or 1000 s to illustrate comparable flow behavior. Therefore, one must explore a range of integration periods to understand the scales of motion before deciding on a representative integration period.

The trajectory mapping framework was applied to analyze the source region of air within the low-level mesocyclone, the forcing of vertical momentum, and the development of vertical vorticity in and near the mesocyclone. Air within the low-level mesocyclone was found to have converged from a broad area surrounding

the circulation, particularly from north of the circulation in a region that had been subjected to subsidence over much of the trajectory integration period. The main updraft was found to have been accelerated by the vertical pressure gradient force over the entire integration period, while other vertical drafts were influenced primarily by precipitation loading and thermal buoyancy. The development of vertical vorticity in the region in and near the mesocyclone was dominated by tilting and stretching. More importantly, however, dissipation from both turbulent mixing and numerical diffusion explained much of the difference between the actual change in vertical vorticity and that computed from the tendency equation following the trajectories. We believe this to be the first study to quantify the integrated impact of numerical and turbulent diffusion on the production of vertical vorticity. The trajectory mapping analysis, therefore, illustrates regions in which calculation of vorticity budgets from individual trajectories may contain significant uncertainty.

The trajectory mapping method was also used to show that prior altitude determined from backward trajectories over a sufficiently long period was a good proxy for equivalent potential temperature. The robustness of the trajectory map was tested by degrading the spatial and temporal resolution of the model output. While individual trajectories may be susceptible to a lack of temporal and spatial resolution, the larger-scale behavior of the trajectory maps did not significantly change when the data frequency and resolved spatial scale were limited to scales typical of research radar datasets. Moreover, the deformation experienced by the trajectories sharpened the spatial scale of the analyses, which may help to match improved temporal resolution from phased array radars. Thus, we are confident that provided a slowly evolving storm (relative to the frequency of the observations), much can be learned from radar-based trajectory maps.

To further elucidate the utility of trajectory maps for observed storms, the prior altitude from 1000-s backward trajectories integrated at three different times was used to evaluate the source regions of air in the mesocyclone of a high-precipitation supercell observed during 29–30 May 2004. The trajectory maps showed the horizontal structure and evolution of descending air parcels for both the rainy downdraft and the rear-flank downdraft. These flow regimes were tracked in time as they wrapped around the mesocyclone, coincident with a period of vortex intensification. Future observational studies using the trajectory mapping framework will examine these downdrafts and their impact on the evolution of the low-level mesocyclone.

Acknowledgments. We thank George Bryan for providing the CM1 model, and Conrad Ziegler, Daniel Dawson, and Brett Roberts for the insightful conversations. Support for this research was provided by National Science Foundation Grant ATM-1063537.

REFERENCES

Adlerman, E. J., K. K. Droegemeier, and R. P. Davies-Jones, 1999: A numerical simulation of cyclic mesocyclogenesis. *J. Atmos. Sci.*, **56**, 2045–2069, doi:10.1175/1520-0469(1999)056<2045:ANSOCM>2.0.CO;2.

Biggerstaff, M. I., and Coauthors, 2005: The Shared Mobile Atmospheric Research and Teaching radar: A collaboration to enhance research and teaching. *Bull. Amer. Meteor. Soc.*, **86**, 1263–1274, doi:10.1175/BAMS-86-9-1263.

Brandes, E. A., 1978: Mesocyclone evolution and tornadogenesis: Some observations. *Mon. Wea. Rev.*, **106**, 995–1011, doi:10.1175/1520-0493(1978)106<0995:MEATSO>2.0.CO;2.

Bruning, E. C., W. D. Rust, D. R. MacGorman, M. I. Biggerstaff, and T. J. Schuur, 2010: Formation of charge structures in a supercell. *Mon. Wea. Rev.*, **138**, 3740–3761, doi:10.1175/2010MWR3160.1.

Bryan, G. H., and J. M. Fritsch, 2002: A benchmark simulation for moist nonhydrostatic numerical models. *Mon. Wea. Rev.*, **130**, 2917–2928, doi:10.1175/1520-0493(2002)130<2917:ABSFMN>2.0.CO;2.

Burgess, D. W., V. T. Wood, and R. A. Brown, 1982: Mesocyclone evolution statistics. Preprints, *12th Conf. on Severe Local Storms*, San Antonio, TX, Amer. Meteor. Soc., 422–424.

Calhoun, K. M., D. R. MacGorman, C. L. Ziegler, and M. I. Biggerstaff, 2013: Evolution of lightning activity and storm charge relative to dual-Doppler analysis of a high-precipitation supercell storm. *Mon. Wea. Rev.*, **141**, 2199–2223, doi:10.1175/MWR-D-12-00258.1.

Dahl, J. M. L., M. D. Parker, and L. J. Wicker, 2012: Uncertainties in trajectory calculations within near-surface mesocyclones of simulated supercells. *Mon. Wea. Rev.*, **140**, 2959–2966, doi:10.1175/MWR-D-12-00131.1.

Doswell, C. A., and P. M. Markowski, 2004: Is buoyancy a relative quantity? *Mon. Wea. Rev.*, **132**, 853–863, doi:10.1175/1520-0493(2004)132<0853:IBARQ>2.0.CO;2.

Dowell, D. C., and H. B. Bluestein, 2002: The 8 June 1995 McLean, Texas, storm. Part I: Observations of cyclic tornadogenesis. *Mon. Wea. Rev.*, **130**, 2626–2648, doi:10.1175/1520-0493(2002)130<2626:TJMTSP>2.0.CO;2.

Emanuel, K. A., 1994: *Atmospheric Convection*. Oxford University Press, 580 pp.

Foote, G. B., and H. W. Frank, 1983: Case study of a hailstorm in Colorado. Part III: Airflow from triple-Doppler measurements. *J. Atmos. Sci.*, **40**, 686–707, doi:10.1175/1520-0469(1983)040<0686:CSOAHI>2.0.CO;2.

French, M. M., H. B. Bluestein, I. PopStefanija, C. Baldi, and R. T. Bluth, 2014: Mobile, phased-array, Doppler radar observations of tornadoes at X band. *Mon. Wea. Rev.*, **142**, 1010–1036, doi:10.1175/MWR-D-13-00101.1.

Gaudet, B. J., and W. R. Cotton, 2006: Low-level mesocyclonic concentration by nonaxisymmetric processes. Part I: Supercell and mesocyclone evolution. *J. Atmos. Sci.*, **63**, 1113–1133, doi:10.1175/JAS3685.1.

Heinselman, P. L., D. L. Priegnitz, K. L. Manross, T. M. Smith, and R. W. Adams, 2008: Rapid sampling of severe storms by the National Weather Radar Testbed phased array radar. *Wea. Forecasting*, **23**, 808–824, doi:10.1175/2008WAF2007071.1.

Isom, B., and Coauthors, 2013: The atmospheric imaging radar: Simultaneous volumetric observations using a phased array weather radar. *J. Atmos. Oceanic Technol.*, **30**, 655–675, doi:10.1175/JTECH-D-12-00063.1.

Johnson, K. W., P. S. Ray, B. C. Johnson, and R. P. Davies-Jones, 1987: Observations related to the rotational dynamics of the 20 May 1977 tornadic storms. *Mon. Wea. Rev.*, **115**, 2463–2478, doi:10.1175/1520-0493(1987)115<2463:ORTTRD>2.0.CO;2.

Klemp, J. B., and R. Rotunno, 1983: A study of the tornadic region within a supercell thunderstorm. *J. Atmos. Sci.*, **40**, 359–377, doi:10.1175/1520-0469(1983)040<0359:ASOTTR>2.0.CO;2.

——, R. B. Wilhelmson, and P. S. Ray, 1981: Observed and numerically simulated structure of a mature supercell thunderstorm. *J. Atmos. Sci.*, **38**, 1558–1580, doi:10.1175/1520-0469(1981)038<1558:OANSSO>2.0.CO;2.

Lemon, L. R., and C. A. Doswell, 1979: Severe thunderstorm evolution and mesocyclone structure as related to tornadogenesis. *Mon. Wea. Rev.*, **107**, 1184–1197, doi:10.1175/1520-0493(1979)107<1184:STEAMS>2.0.CO;2.

Ludlam, F. H., 1963: Severe local storms: A review. *Severe Local Storms*, *Meteor. Monogr.*, No. 27, Amer. Meteor. Soc., 1–30.

Lund, N. R., D. R. MacGorman, T. J. Schuur, M. I. Biggerstaff, and W. D. Rust, 2009: Relationship between lightning location and polarimetric radar signatures in a small mesoscale convective system. *Mon. Wea. Rev.*, **137**, 4151–4170, doi:10.1175/2009MWR2860.1.

MacGorman, D. R., and Coauthors, 2008: TELEX: The Thunderstorm Electrification and Lightning Experiment. *Bull. Amer. Meteor. Soc.*, **89**, 997–1013, doi:10.1175/2007BAMS2352.1.

Mansell, E. R., C. L. Ziegler, and E. C. Bruning, 2010: Simulated electrification of a small thunderstorm with two-moment bulk microphysics. *J. Atmos. Sci.*, **67**, 171–194, doi:10.1175/2009JAS2965.1.

Markowski, P. M., J. M. Straka, and E. N. Rasmussen, 2002: Direct surface thermodynamic observations within the rear-flank downdrafts of nontornadic and tornadic supercells. *Mon. Wea. Rev.*, **130**, 1692–1721, doi:10.1175/1520-0493(2002)130<1692:DSTOWT>2.0.CO;2.

——, and Coauthors, 2012: The pretornadic phase of the Goshen County, Wyoming, supercell of 5 June 2009 intercepted by VORTEX2. Part II: Intensification of low-level rotation. *Mon. Wea. Rev.*, **140**, 2916–2938, doi:10.1175/MWR-D-11-00337.1.

Mashiko, W., H. Niino, and K. Teruyuki, 2009: Numerical simulations of tornadogenesis in an outer-rainband minisupercell of Typhoon Shanshan on 17 September 2006. *Mon. Wea. Rev.*, **137**, 4238–4260, doi:10.1175/2009MWR2959.1.

Miller, L. J., and S. M. Fredrick, 1998: CEDRIC: Custom Editing and Display of Reduced Information in Cartesian Space. Manual, Mesoscale and Microscale Meteorology Division, National Center for Atmospheric Research, 130 pp.

Oye, D., and M. Case, 1995: REORDER: A program for gridding radar data installation and use manual for the Unix version. National Center for Atmospheric Research, 44 pp. [Available online at http://www.eol.ucar.edu/content/reorder-reference-manual.]

Palucki, J. L., M. I. Biggerstaff, D. R. MacGorman, and T. Schuur, 2011: Comparison between low-flash and non-lightning-producing convective areas within a mature mesoscale convective system. *Wea. Forecasting*, **26**, 468–486, doi:10.1175/WAF-D-10-05012.1.

Payne, C. D., T. J. Schuur, D. R. MacGorman, M. I. Biggerstaff, K. Kuhlman, and W. D. Rust, 2010: Polarimetric and electrical characteristics of a lightning ring in a supercell storm. *Mon. Wea. Rev.*, **138**, 2405–2425, doi:10.1175/2009MWR3210.1.

Rotunno, R., and J. B. Klemp, 1982: The influence of the shear-induced pressure gradient on thunderstorm motion. *Mon. Wea. Rev.*, **110**, 136–151, doi:10.1175/1520-0493(1982)110<0136:TIOTSI>2.0.CO;2.

——, and ——, 1985: On the rotation and propagation of simulated supercell thunderstorms. *J. Atmos. Sci.*, **42**, 271–292, doi:10.1175/1520-0469(1985)042<0271:OTRAPO>2.0.CO;2.

Schenkman, A. D., M. Xue, and M. Hu, 2014: Tornadogenesis in a high-resolution simulation of the 8 May 2003 Oklahoma City supercell. *J. Atmos. Sci.*, **71**, 130–154, doi:10.1175/JAS-D-13-073.1.

Shen, Y., and G. Zha, 2010: Improvement of the WENO scheme smoothness estimator. *Int. J. Numer. Methods Fluids*, **64**, 653–675.

Smagorinsky, J., 1963: General circulation experiments with the primitive equations. I. The basic experiment. *Mon. Wea. Rev.*, **91**, 99–164, doi:10.1175/1520-0493(1963)091<0099:GCEWTP>2.3.CO;2.

Wakimoto, R. M., C. Liu, and H. Cai, 1998: The Garden City, Kansas, storm during VORTEX 95. Part I: Overview of the storm life cycle and mesocyclogenesis. *Mon. Wea. Rev.*, **126**, 372–392, doi:10.1175/1520-0493(1998)126<0372:TGCKSD>2.0.CO;2.

Wicker, L. J., and R. B. Wilhelmson, 1995: Simulation and analysis of tornado development and decay within a three-dimensional supercell thunderstorm. *J. Atmos. Sci.*, **52**, 2675–2703, doi:10.1175/1520-0469(1995)052<2675:SAAOTD>2.0.CO;2.

Ziegler, C. L., 1985: Retrieval of thermal and microphysical variables in observed convective storms. Part I: Model development and preliminary testing. *J. Atmos. Sci.*, **42**, 1487–1509, doi:10.1175/1520-0469(1985)042<1487:ROTAMV>2.0.CO;2.

——, 2013: A diabatic Lagrangian technique for the analysis of convective storms. Part I: Description and validation via an observing system simulation experiment. *J. Atmos. Oceanic Technol.*, **30**, 2248–2265, doi:10.1175/JTECH-D-12-00194.1.

——, E. N. Rasmussen, T. R. Shepherd, A. I. Watson, and J. M. Straka, 2001: The evolution of low-level rotation in the 29 May 1994 Newcastle–Graham, Texas, storm complex during VORTEX. *Mon. Wea. Rev.*, **129**, 1339–1368, doi:10.1175/1520-0493(2001)129<1339:TEOLLR>2.0.CO;2.